Gas Jet–Workpiece Interactions in Laser Machining

Kai Chen

Y. Lawrence Yao

Vijay Modi

Department of Mechanical Engineering,
Columbia University,
New York, NY 10027

Laser machining efficiency and quality are closely related to gas pressure, nozzle geometry, and standoff distance. Modeling studies of laser machining rarely incorporate gas effects in part because of the complex structure and turbulent nature of jet flow. In this paper, the interaction of a supersonic, turbulent axisymmetric jet with the workpiece is studied. Numerical simulations are carried out using an explicit, coupled solution algorithm with solution-based mesh adaptation. The model is able to make quantitative predictions of the pressure, mass flow rate as well as shear force at the machining front. Effect of gas pressure and nozzle standoff distance on structure of the supersonic shock pattern is studied. Experiments are carried out to study the effect of processing parameters such as gas pressure and standoff distance. The measured results are found to match and hence validate the simulations. The interaction of the oblique incident shock with the normal standoff shock is found to contribute to a large reduction in the total pressure at the machining front and when the nozzle pressure is increased beyond a certain point. The associated reduction in flow rate, fluctuations of pressure gradient and shear force at the machining front could lower the material removal capability of the gas jet and possibly result in a poorer surface finish. The laser cutting experiments show that the variation of cut quality are affected by shock structures and can be represented by the mass flow rate. [S1087-1357(00)01702-0]

1 Introduction

The assist gas plays an important role in laser machining. It provides a mechanical force to eject the melt from the cut zone and cools the cut zone by forced convection. Inefficient removal of the molten layer can lead to deterioration in cut quality. When the gas is reactive, it also delivers additional exothermic energy to assist in machining. Hence the efficiency and overall quality of laser machining is strongly dependent on the interaction of the gas jet with the workpiece.

The role of oxygen pressure in laser cutting of steels was studied experimentally by Ivarson et al. [1]. They found that there are two optimum pressure ranges where the cut quality is good. Numerical calculations of the three-dimensional turbulent oxygen jet by O'Neill and Steen [2] showed that entrainment of impurities occurs inside the cut kerf and this can have detrimental effects on oxidation and cutting capability. The use of an off-axis nozzle in tandem with a coaxial nozzle was investigated by Chryssolouris and Choi [3], and the use of a single off-axis nozzle was studied experimentally by Brandt and Settles [4]. Other supersonic nozzle configurations have also been considered to improve the effects of gas jet [5–8]. A comprehensive review of the gas jet effects was presented by Fieret et al. [9], in which a Mach shock was found to reduce the stagnation pressure at the workpiece and to encourage the formation of a stagnation bubble on the surface of the workpiece. There is however little theoretical work to systematically study the effects of a gas jet and process parameters such as nozzle position and gas pressure.

In industrial practice, nozzles are positioned close to the workpiece and nozzle pressures are chosen within a certain range. For a convergent nozzle, the flow downstream of the nozzle exit becomes supersonic if the upstream total reservoir pressure is greater than 1.89 bar [9], a condition common to laser machining. In other words, the jet is underexpanded if the total pressure exceeds 1.89 times the ambient pressure. The ratio between the jet exit and ambient static pressures is called the underexpansion ratio. Downstream of the nozzle exit, oblique shock cells are formed. Their intensity and interaction with the standoff shock on the workpiece surface depends on the nozzle pressure and the nozzle standoff distance. This interaction to an extent determines the effects of the gas jet inside the cut kerf.

Turbulent underexpanded free jets and their impingement on a plate have been extensively studied because of their wide range of applications. Experimental and analytical studies have examined the shock behavior of free jets. At underexpansion ratios below 3 to 4 (referred to as ''moderately underexpanded jets'') pressure equilibrium is achieved through a series of repetitive oblique shock cells, which eventually decay into a conventional constant-pressure jet (Fig. 1*a*). For underexpansion ratios greater than 3-4 (referred to as ''highly underexpanded''), however, the first shock cells contain normal shock waves or a Mach disk [10,11] and the location of the Mach disk can be analytically predicted [12]. The normal impingement of an underexpanded jet onto a flat plate located within the first few shock cells leads to the formation of a well-defined standoff shock upstream off the plate. Across the standoff shock, the jet suddenly decelerates to subsonic flow and is then deflected by the plate [13]. A sonic line divides the jet on the plate surface into two regions: one is a shock layer above the stagnant point and the other is a wall jet region which consists of compression/expansion waves that originate from the upper part of the sonic line (Fig. 1*b*). Their detailed structure was studied by Gummer and Hunt [14] and Carling and Hunt [13]. They report that in some cases underneath the Mach disk, a vortex ring or stagnation bubble may form. This could be a result of the interaction of the jet shock with the normal standoff shock [15] or a result of the weak shock waves (due to nozzle imperfections) interacting with the standoff shock [16]. The stagnation bubble may lead to ineffective debris removal and along with absorption of laser radiation may lead to plasma formation [17]. Since most laser machining operates at a total pressure between 3 to 5 bar, i.e. in the range of moderately underexpanded jets to the onset of highly underexpanded jet, the above described findings are helpful in understanding the flow structure present in laser machining.

The current effort aims at examining the gas jet effects by carrying out numerical simulations and experiments for a geometry that closely mimics the real machining case. The effects of processing parameters such as gas pressure and nozzle standoff distances on cut quality are examined. Simulations are first validated

Contributed by the Manufacturing Engineering Division for publication in the JOURNAL OF MANUFACTURING SCIENCE AND ENGINEERING. Manuscript received Sept. 1998; revised Nov. 1999. Associate Technical Editor: K. Ehmann.

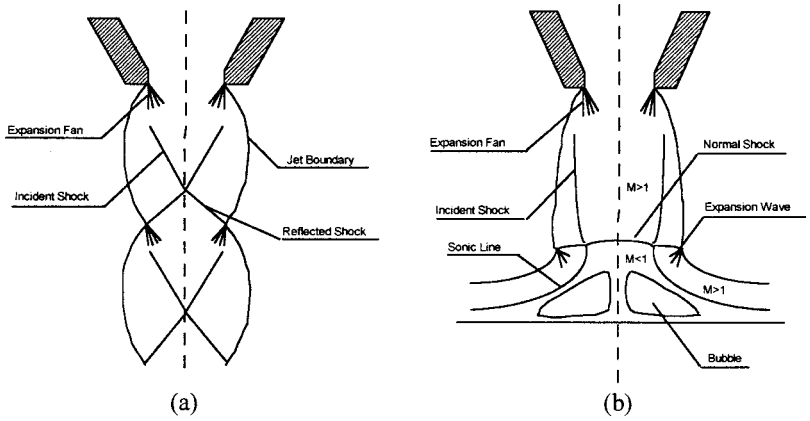

Fig. 1 Schematic of underexanded (*a*) free jet and (*b*) impinging jet

against several well documented free jet and impinging jet cases, for which experimental data exists. The validity of the simulation results is further supported by the experimental investigation.

2 Numerical Simulations

2.1 Assumptions. In order to make the problem amenable to analysis while addressing the main goals of the paper, the following assumptions are made:

A conical convergent nozzle is assumed to deliver a gas jet that normally impinges onto a workpiece plate with a through hole concentric with the nozzle (Fig. 2). The through hole diameter d is assumed to be smaller than the exit diameter of nozzle D. The assumption of a through hole that is concentric with the nozzle makes the problem axisymmetric, thus reducing the dimensionality of the problem. Axisymmetric studies have significance not only because they correspond to the laser drilling case, but because they also reveal the generic behavior of the gas flow upstream of the machining front. This flow behavior is expected to be relatively independent of the actual cut geometry.

The thermal interactions of the laser and the possibly reactive gas with workpiece material including melting and vaporization are not considered. In other words, the hole diameter is prescribed unlike a real machining process where the size of the hole or cut would be determined by the operating conditions. The gas flow structure and the mass flow rate through the hole are primarily determined by the total pressure upstream of the hole, which in turn is determined by the interaction between the nozzle, workpiece and gas flow.

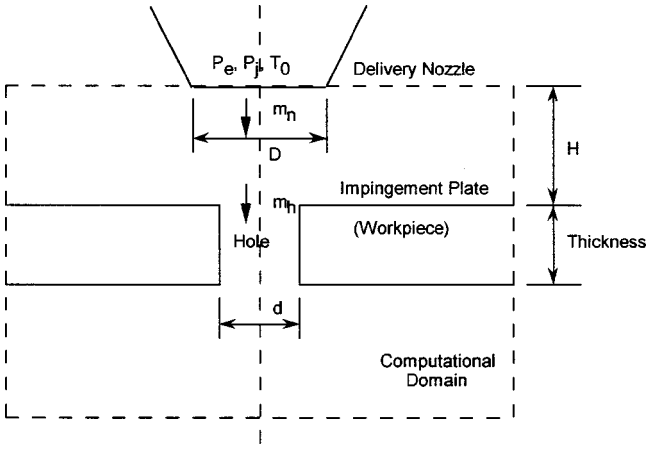

Fig. 2 Schematic of computational domain for simulations

2.2 Governing Equations. The flow is assumed to be governed by the steady compressible Reynolds-Averaged Navier-Stokes (RANS) equations. A two-equation turbulence model based on the Renormalization Group k-ε (RNG) theory is utilized [18]. In axisymmetric coordinates the RANS equations can be written as

$$\frac{\partial(\mathbf{F}-\mathbf{F}_v)}{\partial x}+\frac{\partial(\mathbf{G}-\mathbf{G}_v)}{\partial r}=0. \tag{1}$$

In the above form (F,G) and (F_v,G_v) represent the inviscid and viscous flux terms respectively.

$$\mathbf{F}=r\begin{bmatrix}\rho u\\ \rho u^2+p\\ \rho uv\\ (\rho e+p)u\end{bmatrix},\quad \mathbf{G}=r\begin{bmatrix}\rho v\\ \rho uv\\ \rho v^2+p\\ (\rho e+p)v\end{bmatrix},$$

$$\mathbf{F}_v=r\begin{bmatrix}0\\ \tau_{xx}\\ \tau_{xr}\\ u\tau_{xx}+v\tau_{xr}\end{bmatrix},\quad \mathbf{G}_v=r\begin{bmatrix}0\\ \tau_{xr}\\ \tau_{rr}\\ u\tau_{rx}+v\tau_{rr}\end{bmatrix}, \tag{2}$$

where u, v are gas velocity in x and r direction. ρ is the density and p is the static pressure. The stress terms in axisymmetric coordinates are

$$\tau_{xx}=\mu\left[2\frac{\partial u}{\partial x}-\frac{2}{3}\left(\frac{1}{r}\frac{\partial}{\partial r}(rv)+\frac{\partial u}{\partial x}\right)\right],$$

$$\tau_{rr}=\mu\left[2\frac{\partial v}{\partial r}-\frac{2}{3}\left(\frac{1}{r}\frac{\partial}{\partial r}(rv)+\frac{\partial u}{\partial x}\right)\right], \tag{3}$$

$$\tau_{xr}=\tau_{rx}=\mu\left[\frac{\partial u}{\partial r}+\frac{\partial v}{\partial x}\right],$$

where τ_{xx} and τ_{rr} are normal stress, and τ_{rx} and τ_{xr} are shear stress. The effective viscosity μ is composed of the molecular viscosity μ_m and the turbulent viscosity μ_t, i.e. $\mu=\mu_m+\mu_t$, and is assumed to be:

$$\mu=\mu_m\left[1+\sqrt{\frac{C_\mu}{\mu_m}}\frac{k}{\sqrt{\varepsilon}}\right]^2. \tag{4}$$

The model constant C_μ is derived analytically by the RNG theory and is 0.0845. In order to obtain μ and μ_t, a two-equation turbulence model (RNG) for turbulent kinetic energy (k) and energy dissipation (ε) is applied. The density and the total internal energy (e) assuming ideal gas behavior are

$$e=\frac{p}{\rho(\gamma-1)}+\frac{1}{2}(u^2+v^2), \quad \text{and} \quad \rho=\frac{p}{RT}, \tag{5}$$

where γ is the specific heat ration.

The equations and relationships outlined in the section provide a set of equations with the primary variables of ρ, p, u, v, k and ε. A commercial computational fluid dynamic (CFD) code, RAMPANT is used to solve these equations.

2.3 Numerical Scheme. The flow solver is an unstructured finite-volume code with the capability of adaptive grid refinement. The solver uses a semi-discrete finite-volume formulation, resulting in a consistent approximation to the conservation laws in integral form

$$\int_S [(\mathbf{F}-\mathbf{F}_v)dr-(\mathbf{G}-\mathbf{G}_v)dx]=0. \tag{6}$$

The spatially discretized form of these equations is obtained by subdividing the physical domain into small cells and applying integral equations to each cell. The discrete, inviscid flux vectors (**F** and **G** in Eq. (6)) are evaluated by flux difference splitting [19]. The discretized equations are obtained by integrating the governing equations over each finite volume. Integration to steady state is carried out using a multi-stage Runge-Kutta scheme with multigrid convergence acceleration.

Nonequilibrium wall functions are used for near wall treatment in conjunction with the RNG turbulence model. Nonequilibrium wall functions extend the applicability of the wall function approach by including the effects of pressure gradient and strong nonequilibrium and hence are suitable for jet impingement. Unstructured triangular grids were generated so that for the wall adjacent cells, the cell dimension is about 30 y^+ in wall units. Here y^+ is defined as $y^+=\rho u_\tau y/\mu$, where u_τ is the local friction velocity and y the physical distance away from the wall. Solution based grid refinements are carried out to the unstructured mesh wherever there are large gradients in the solution variables.

2.4 Boundary Conditions. Since the delivery nozzle is a convergent type and the flow at the nozzle exit is always choked for pressures of interest, our computational domain boundary is located at the nozzle exit plane. The flow at the nozzle exit is assumed to be uniform and at sonic conditions. Whereas this may cause some inaccuracies particularly close to the nozzle lip, it will not influence the flow characteristic downstream. Sonic conditions are enforced at the nozzle lip by specifying the total pressure and total temperature according to one-dimensional isentropic flow relations:

$$\frac{p_0}{p_s}=\left[1+\frac{\gamma-1}{2}M^2\right]^{\gamma/\gamma-1}, \tag{7}$$

$$\frac{T_0}{T}=1+\frac{\gamma-1}{2}M^2, \tag{8}$$

where the Mach number M is set to unity. p_0 and T_0 are static pressure and temperature respectively. At inlet boundaries the total pressure, static pressure, total temperature and the flow direction are imposed. At the subsonic outlet boundary, the static pressure is specified whereas the remaining flow properties are extrapolated. No-slip wall and symmetry boundary conditions are applied at the plate and the centerline respectively.

3 Model Experimental Setup

The experimental setup was designed to measure the mass flow rate through a predrilled hole in the workpiece with variation of total nozzle pressure and standoff distance. While the mass flow rate through the cut kerf may not be of concern in itself for laser machining, it is directly related to the total pressure at the machining front which in turn is an important factor in determining the material removal capability of the gas jet. The measurement of the mass flow rate also provides a convenient and viable verification of the simulation results. Considering the small physical dimension of the actual laser kerf, field measurement of the flow would be very difficult.

A schematic of the experimental setup is shown in Fig. 3. A commercial sonic (converging-only) nozzle with a nozzle diameter D of 1.35 mm is used. Compressed air from a gas tank is fed into the nozzle through a gas inlet where a pressure gauge was set. The gas pressure can be adjusted through a regulator installed upstream of the gas inlet. The gas exiting the nozzle impinges on plate (or workpiece) with a predrilled hole in it. The impingement plate is 1.5 mm thick with two through holes (with diameters 0.508 mm or 0.711 mm). The nozzle flow $\dot{m}_n$ is in part deflected by the plate. The remaining flow, through hole flow $\dot{m}_h$ enters the hole. The small hole diameter and the high gas speeds make it difficult to measure the through flow. Hence a collection box is placed directly underneath to collect the flow and direct it to a 10 mm measurement nozzle (area $A_m=78.5\,\text{mm}^2$) at considerably lower flow speed. The impingement plate along with the collection box are placed on a precision x-y table to allow alignment of the hole with the delivery nozzle. A micrometer is used to obtain a precise measurement of the stand-off distance. The velocity of the gas leaving the measurement nozzle (V_m) is then measured using a hot-film anemometer (TSI 8350). The hot-film probe is placed directly underneath the measurement nozzle exit by another positioning system for accurate centering. The measurement nozzle contour guarantees that the velocity profile of the gas stream is nearly uniform. The density of the gas leaving the measurement nozzle ρ_m is assumed to be that of an ideal gas at ambient conditions. The mass flow rate through the measurement nozzle ($\rho_m A_m V_m$) and hence the through hole flow $\dot{m}_h$ is obtained.

The hot-film anemometer was calibrated using a pitot tube in the 40 mm×230 mm test section of a wind tunnel. The pitot tube pressure was obtained with the assistance of a Barocell electronic pressure gauge calibrated to 0.2 inches of water per unit volt. The output was measured using a data acquisition card on PC. A least square linear fit line was used to obtain the numerical values for the velocities read from the hot-film velocimeter.

Since the flow at the throat of the delivery nozzle is always choked, it is possible to relate the upstream total pressure p_t to the mass flow rate from the nozzle $\dot{m}_n$. The following relationship holds at the sonic nozzle exit

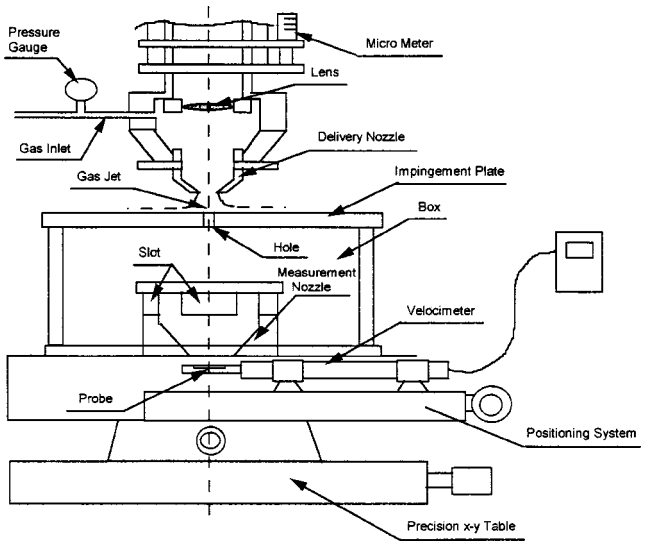

Fig. 3 Schematic of experimental setup

$$\dot{m}_n = c_D A p_t \left[\left(\frac{2}{RT} \right) \left(\frac{\gamma}{\gamma+1} \right) \left(\frac{2}{\gamma+1} \right)^{2/\gamma-1} \right]^{1/2}, \quad (9)$$

where $p_t = P_e + P_a$. P_e is the total gauge pressure at the nozzle exit, P_a is the ambient pressure and A is area at the nozzle exit. The total pressure thus can be obtained by knowing the mass flow rate from the sonic nozzle. In the above relationship, the mass flow rate is corrected for viscous losses using a nozzle discharge coefficient c_D. The coefficient c_D is estimated to be 0.988 based on nozzle-throat Reynolds number for the nozzle used here [20].

The same experimental apparatus was used to measure the mass flow rate from the sonic nozzle. The collection box however was raised to let the delivery nozzle lip stick into the box and the gap was sealed to prevent leakage. Thus the mass flow rate from the sonic nozzle can be obtained in the same manner as described before.

The experimental uncertainties in the measurement quantities are either due to uncertainties in the primary measurements or a composite uncertainty due to several measurements. The uncertainty analysis follows the standard experimental method [21]. The estimated uncertainties are listed in the following table:

Quantity	A_m	ρ_m	V_m	$\dot{m}_h$ or $\dot{m}_n$
Uncertainty	±3%	±2%	±6%	±7%

Quantity	T	A	c_D	H	P_e
Uncertainty	±2%	±3%	±0.3%	±0.5%	±8%

4 Code Validation Studies

To validate the CFD solver, two complex test cases for which reliable experimental data exists were used. These test cases were related to ascertain the ability of the solver to capture both free and impinging jet behavior of the flow of interest.

In Test Case 1, a supersonic moderately underexpanded jet exhausting into otherwise stagnant air was examined. The underexpansion ratio (P_j/P_a) was 1.45, and the exit Mach number M_j was 2. For the case of moderate underexpansion, as the gas leaves the nozzle exit, it goes through a Prandtl-Meyer expansion to the ambient pressure at the jet boundary. The expansion waves are reflected as compression waves at the jet boundary. These compression waves coalesce to form an incident shock wave. The incident shock wave meets at the symmetry centerline, where it reflects to form a reflected wave. The oblique reflected wave is again reflected from the free jet boundary as expansion waves. The repetition of this process produces a well-known diamond wave pattern (Fig. 1*a*). For a quantitative comparison, the measurements of the streamwise pressure variation along the jet centerline by Seiner & Norum [22] are shown in Fig. 4 along with our computations. The agreement is quite good for the first few cells indicating that the compressibility effects and the damping of wave strength due to turbulent dissipation are properly modeled.

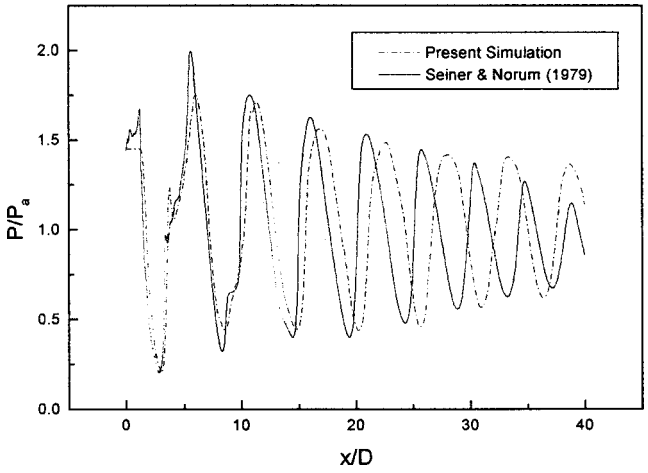

Fig. 4 Comparison of computed and measured streamwise pressure variation along a free jet axis for $M_j = 2.0$ and $P_j/P_a = 1.45$

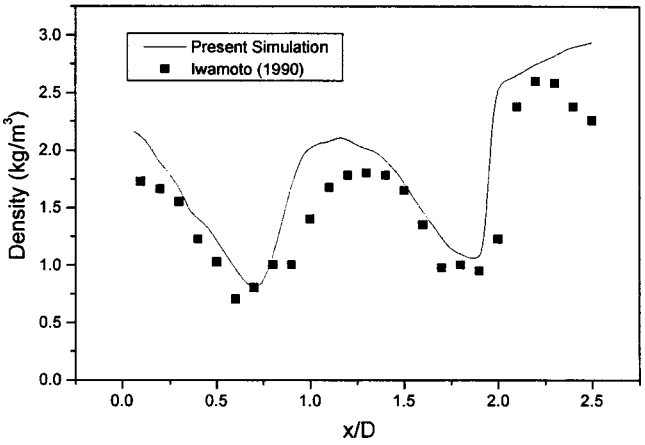

Fig. 5 Comparison of computed and measured streamwise density variation along an impinging jet axis for $M_j = 1.0$, $P_j/P_a = 3.0$ and $H/D = 2.5$

In Test Case 2, a supersonic jet impinging normally on a flat plate ($M_j = 1.0$, $P_j/P_a = 3.0$, $H/D = 2.5$) was examined. Among other things the streamwise density variation along the jet axis was measured. When a plate is placed in the path of a supersonic jet, a stagnation region is formed at some distance away from the solid surface. A normal shock forms off the plate allowing gas flow to decelerate to subsonic values. The pressure rises to above ambient pressure in the subsonic region (Fig. 1*b*). Computed streamwise density variation along jet axis is compared with the measurements of Iwamoto [23] (Fig. 5). The agreement indicates that CFD solver is able to capture the structure of the incident and the normal shock in the case of jet impingement. The RNG model, however, is not accurate in predicting the flow behavior very close to the stagnation point. This is probably responsible for the divergence between predicted values and experimental data in the region close to impinging plate.

5 Mass Flow Rate Experimental Results

The objective of the experimental part of this study was to determine the effects of hole diameter d, standoff distance H and total pressure p_t on the hole through flow $\dot{m}_h$. Two sets of measurements were carried out. For Group 1 experiments, the total gauge pressure at nozzle exit P_e was varied continuously between 120 kPa and 490 kPa for $d = 0.711$ and 0.508 mm and for standoff distance $H = 1.0$, 1.5 and 2.0 mm. For Group 2 experiments however, three distinct values of P_e were chosen and H was varied continuously from 0 to 3.5 mm for $d = 0.711$ and 0.508 mm. The above described conditions are summarized in the following table:

	d (mm)		H (mm)			P_e (kPa)		
Group 1	0.711	0.508	1.0	1.5	2.0	Varied from 120 to 490		
Group 2	0.711	0.508	Varied from 0 to 3.5			125	243	363

The measured $\dot{m}_h$ data are shown in Fig. 6*a* and Fig. 6*b* for Group 1 experiments. For $H = 1.0$ mm, $\dot{m}_h$ is found to mono-

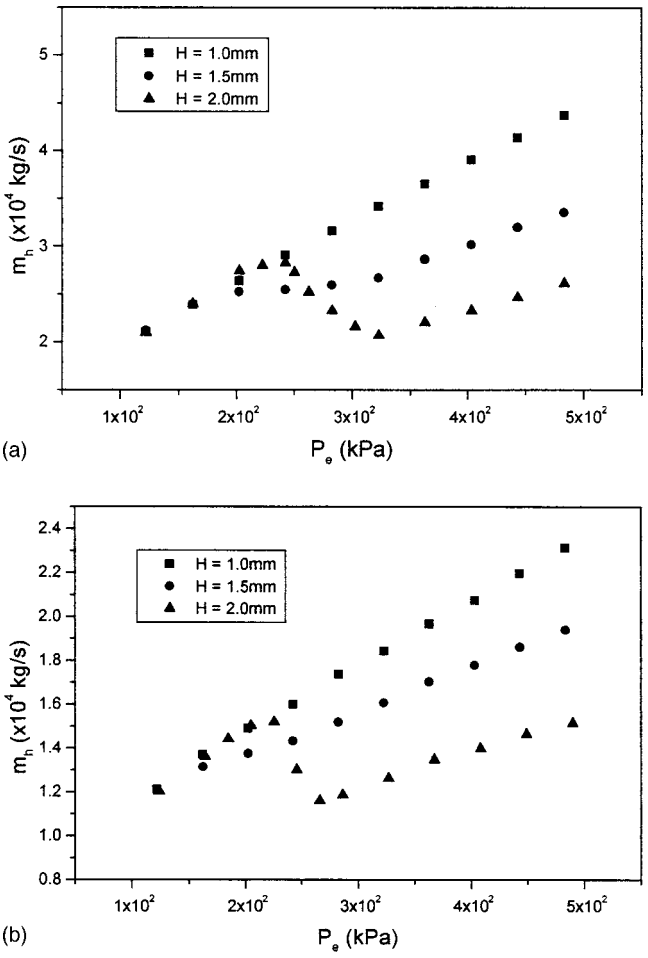

Fig. 6 (*a*) Measured through-hole mass flow rate with total gauge pressure for $d=0.711$ mm. (*b*) Measured through-hole mass flow rate with total gauge pressure for $d=0.508$ mm.

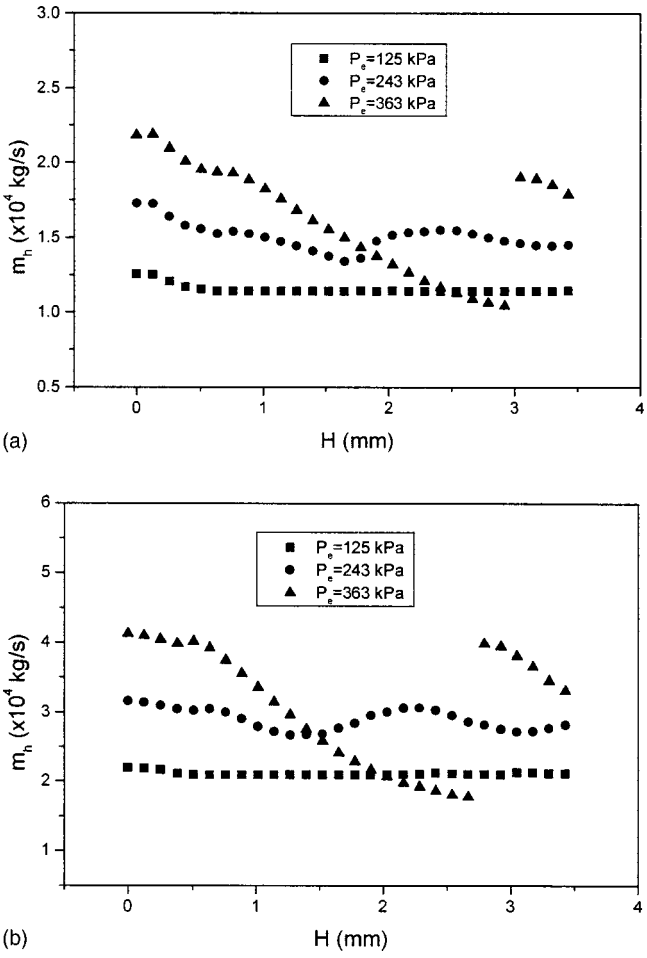

Fig. 7 (*a*) Measured through-hole mass flow rate vs. nozzle standoff distance for $d=0.711$ mm. (*b*) Measured through-hole mass flow rate vs. nozzle standoff distance for $d=0.508$ mm.

tonically and linearly increase with P_e. For $H=2.0$ mm however, $\dot{m}_h$ first increases with total pressure until it reaches a local maximum at $P_e=240$ kPa for $d=0.711$ mm and $P_e=225$ kPa for $d=0.508$ mm, respectively. The mass flow rate then reduces even as total pressure increases, until it reaches a local minimum and begins to increase again. For $H=1.5$ mm, $\dot{m}_h$ behavior lies in-between those for $H=1$ and 2 mm, and the local maximum and minimum are not evident. The $\dot{m}_h$ profiles for the two different hole sizes are qualitatively similar, indicating that hole diameter may not be an important factor for the study of flow behavior, as long as the hole diameter d is much smaller than the nozzle diameter D. Since one would expect $\dot{m}_h$ to monotonically increase with P_e, the unusual behavior for $H=2.0$ mm implies that a change in shock structure can have a significant effect on flow behavior. This will be further explained in conjunction with simulation results later.

Figures 7*a* and 7*b* show the measured $\dot{m}_h$ data for Group 2 experiments. At P_e values of 125 kPa and 243 kPa, $\dot{m}_h$ is relatively unaltered with changes in H, indicating that the flow structure remains unchanged along the centerline. However, for a higher P_e value of 363 kPa, $\dot{m}_h$ reduces continuously until a critical standoff distance, H_{critical} of about 3 mm is reached. At H_{critical} a small increase in standoff distance results in a large jump in $\dot{m}_h$. Beyond this point $\dot{m}_h$ continues to decrease with increasing H. The critical point is accompanied with strong shock noises heard during the experiments. This behavior is essentially repeated for a hole size of $d=0.508$ mm.

6 Simulation Results

Flow behavior within the hole as well as $\dot{m}_h$ are essentially determined by the total gas pressure immediately upstream of the hole. This pressure is nearly equal to the total pressure downstream of the normal standoff shock. It is desirable to minimize the total pressure loss through the normal shock. This can be achieved by changing the shock structure, as will be shown by the simulation results. The simulations were carried out over the computational domain shown in Fig. 2 for the same operating pressure conditions as the experiments.

The velocity field across the hole is integrated to obtain a computed value of $\dot{m}_h$. The variations of the computed and measured $\dot{m}_h$ with P_e are shown in Fig. 8. The computed results follow the trends in the experimental results closely and capture the local maximum/minimum in $\dot{m}_h$ for $H=2$ mm. The experimental uncertainties in the measurements are shown as error bars in Fig. 8. The variation in the computed and measured $\dot{m}_h$ with H is shown in Fig. 9 with uncertainties reflected in Fig. 8.

To further understand the particular phenomena seen in Fig. 8, contours of static pressure at two different nozzle pressure levels for $H=2$ mm and $d=0.711$ mm are shown in Fig. 10. The oblique and the normal standoff shocks are similar to those of a gas jet impinging on a flat plate. At the lower P_e of 207 kPa in Fig. 10*a*, the oblique shock has a larger deflection angle as expected from the theory of oblique shock waves [9]. The incident shock waves meet at the centerline and are reflected prior to interacting with the normal standoff shock. In this case, the total pressure decrease

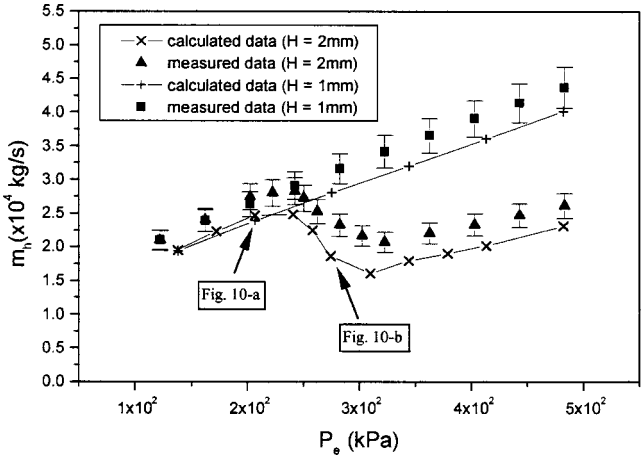

Fig. 8 Computed and measured through-hole mass flow rate for $d=0.711$ mm

downstream of the normal standoff shock is not large. At a higher P_e of 276 kPa in Fig. 10*b*, the incident shock waves have a smaller deflection angle thus preventing them to meet and reflect before interacting with the normal standoff shock. In this case, the total pressure decreases dramatically downstream of the normal standoff shock.

As Abbett [12] points out, a normal shock is formed due to a strong compression process when the flow traverses from subsonic to supersonic region. The strength of the normal shock is related to the extent of the compression. Regular reflection of the oblique shock from the axis may result in a static pressure rise large enough so that additional compression is not significant. In this case, the normal shock is weak. On the contrary, if the oblique shock directly interacts with the normal shock, significant compression is needed in order to establish the pressure necessary for the subsonic region. In that case, the normal shock is much stronger. The corresponding total pressure loss as flow crosses the normal shock is large if the shock strength is high, and small if low.

It is not surprising that the total pressure at which the incident shock waves meet the centerline (about 225 kPa) and touch the standoff shock corresponds to the a local maximum in Fig. 8 for $H=2$ mm. Beyond that critical point, the mass flow rate decreases in spite of increasing gas pressure because of the total pressure

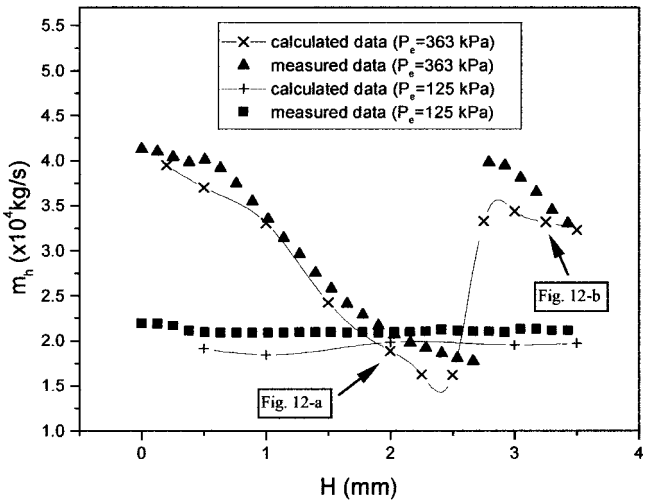

Fig. 9 Computed and measured through-hole mass flow rate for $d=0.711$ mm

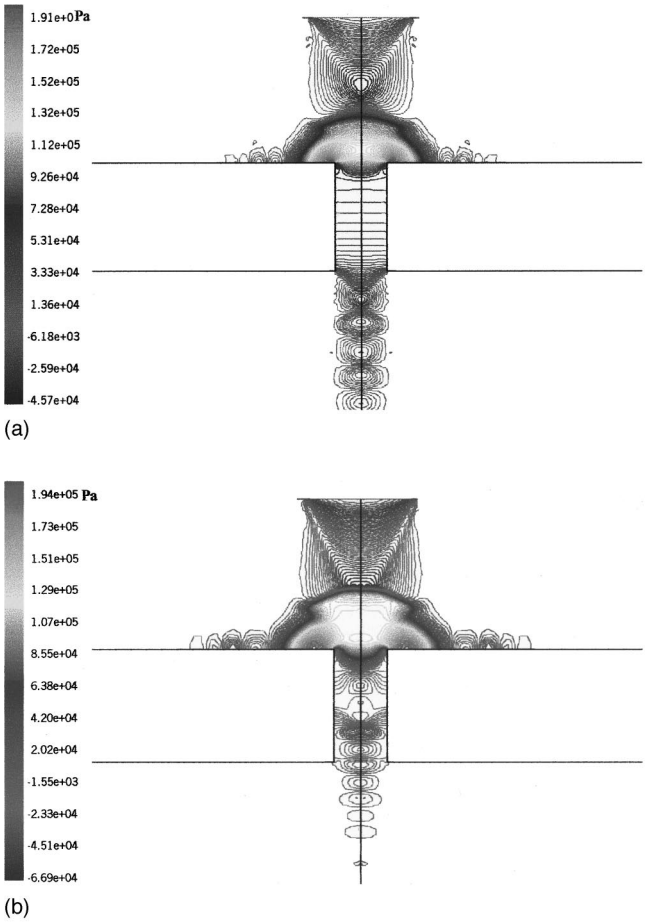

Fig. 10 (*a*) Contour of static pressure for $P_e=207$ kPa ($d=0.711$ mm, $H=2$ mm). (*b*) Contour of static pressure for $P_e=276$ kPa ($d=0.711$ mm, $H=2$ mm).

loss. The reason that the decrease is gradual instead of a sudden drop at a single P_e is due to the expansion of the normal standoff shock once the oblique shock directly interacts with the standoff shock, resulting in decreased shock strength. A slight increase of the nozzle pressure will increase the standoff shock strength and the loss of the total pressure. Thus the total pressure after standoff shock will decrease until the nozzle pressure is high enough to offset the pressure loss. For the case of small H (e.g., 1 mm), the oblique shock always interacts with the standoff shock directly and therefore the total pressure after the standoff shock increases with the nozzle pressure and the through-hole mass flow rate always increases with the nozzle pressure.

The aforementioned explanation is confirmed by the axial variation of total pressure shown in Fig. 11 for different nozzle pressures. The total pressure loss at higher nozzle pressures is so large that in fact the total pressure downstream of the standoff shock for a P_e of 276 kPa is less than that for a lower P_e of 258 kPa. The loss increases even further with P_e so that the total pressure downstream of the standoff shock for $P_e=345$ kPa is nearly the same as that for P_e of 276 kPa.

Figures 12*a* and 12*b* show the contours of static pressure, for $H=2$ and 3.25 mm, corresponding to two standoff distances before and after the jump in $\dot{m}_h$ seen in Fig. 10 with P_e of 363 kPa. In Fig. 12*a* ($H=2.0$ mm), the incident shock interacts with the normal standoff shock directly. For low values of H, the through-hole mass flow rate decreases as the standoff distance increases as long as the incident shock directly meets the standoff shock. However, when the standoff distance reaches a point where the incident shock waves first meet at the centerline before they reflect

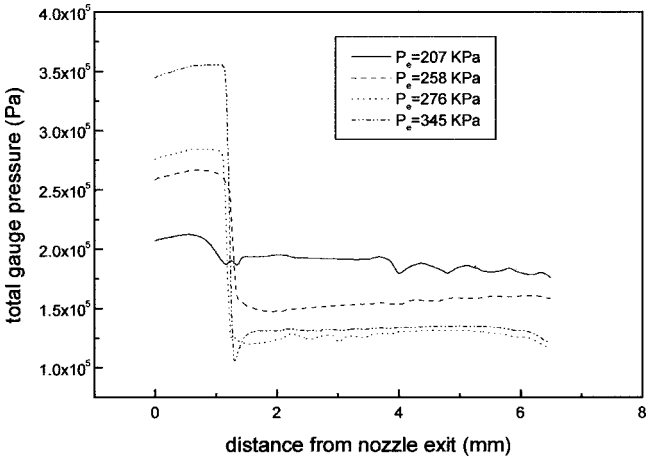

Fig. 11 Computed variation of total pressure along the centerline for $H=2.0$ mm and $d=0.711$ mm

and interact with the normal shock, the loss of total pressure is greatly reduced, which results in a jump of the through-hole mass flow rate (Fig. 12*b*).

In most laser machining cases, the nozzle standoff distance is chosen to be 0.5 mm—1.5 mm, thus the incident shock will always interact with the standoff shock directly. However, this study reveals that some favorable operating conditions do exist for

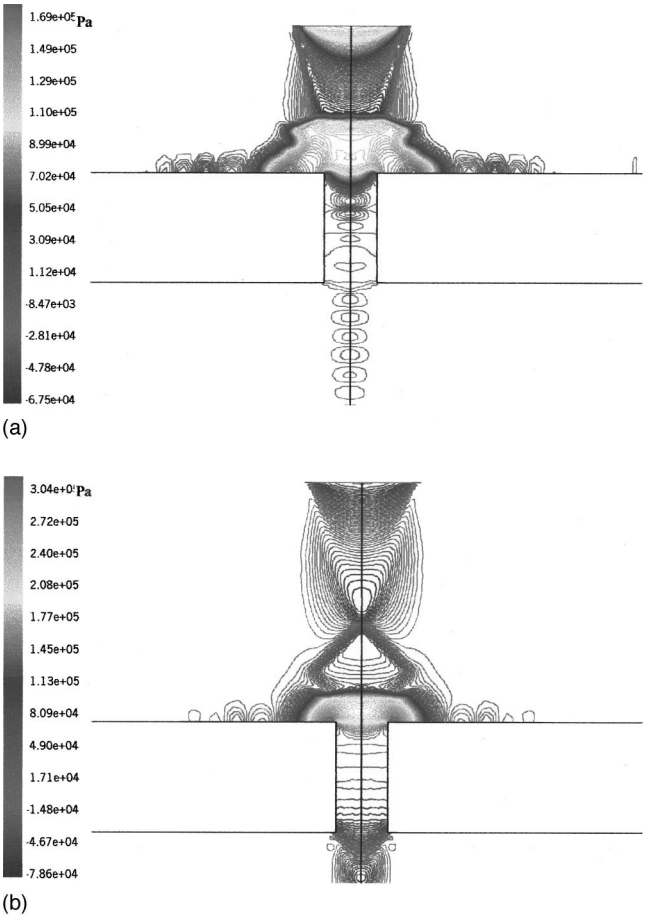

Fig. 12 (*a*) Contour of static pressure for $H=2$ mm ($d=0.711$ mm, $P_e=363$ KPa). (*b*) Contour of static pressure for $H=3.25$ mm ($d=0.711$ mm, $P_e=363$ KPa).

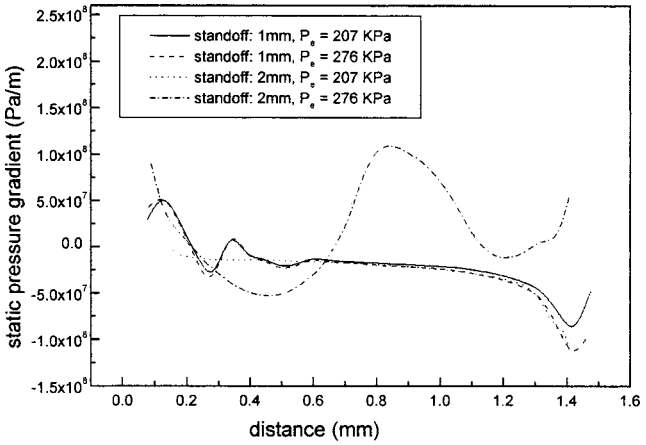

Fig. 13 Static pressure gradient inside hole

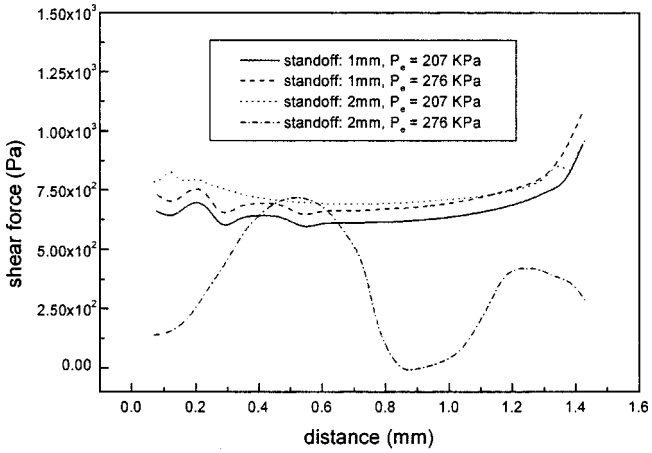

Fig. 14 Shear force inside hole

large nozzle standoff distances within a certain range of the nozzle pressure. In those situations, the reflected shock is produced and interacts with the standoff shock, which has a higher total pressure downstream of the standoff shock. The nozzle pressure should be chosen to avoid direct contact between the incident shock and the standoff shock for large nozzle standoff distances.

The low total pressure after the standoff shock is associated with fluctuations of the pressure gradient and shear stress inside the hole. Figures 13 and 14 show the static pressure gradient and the shear force inside the hole for four different conditions. Large fluctuations in the pressure gradient and the shear force for $Pe=276$ kPa and $H=2$ mm corresponds to a characteristic behavior of that shown in Fig. 10*b*, where the incident shock has direct contact with the normal standoff shock. Since the pressure gradient and the shear force are two driving forces in melt removal, the fluctuation has detrimental effects on the removal capability of the gas jet, which often results in poorer cut quality.

7 Laser Cutting Experimental Results

As pointed out previously, the mass flow rate associated with the shock structure is primarily determined by the interactions between nozzle, workpiece and gas flow. It is expected that the laser cut quality is affected by the change of shock structure with varying gas pressure and standoff, as it was numerically predicted. To verify the gas jet effects in laser cut quality, cutting experiments of lasers were performed. Unlike the idealized axisymmetric case, the linear cut kerf of laser cutting renders the problem

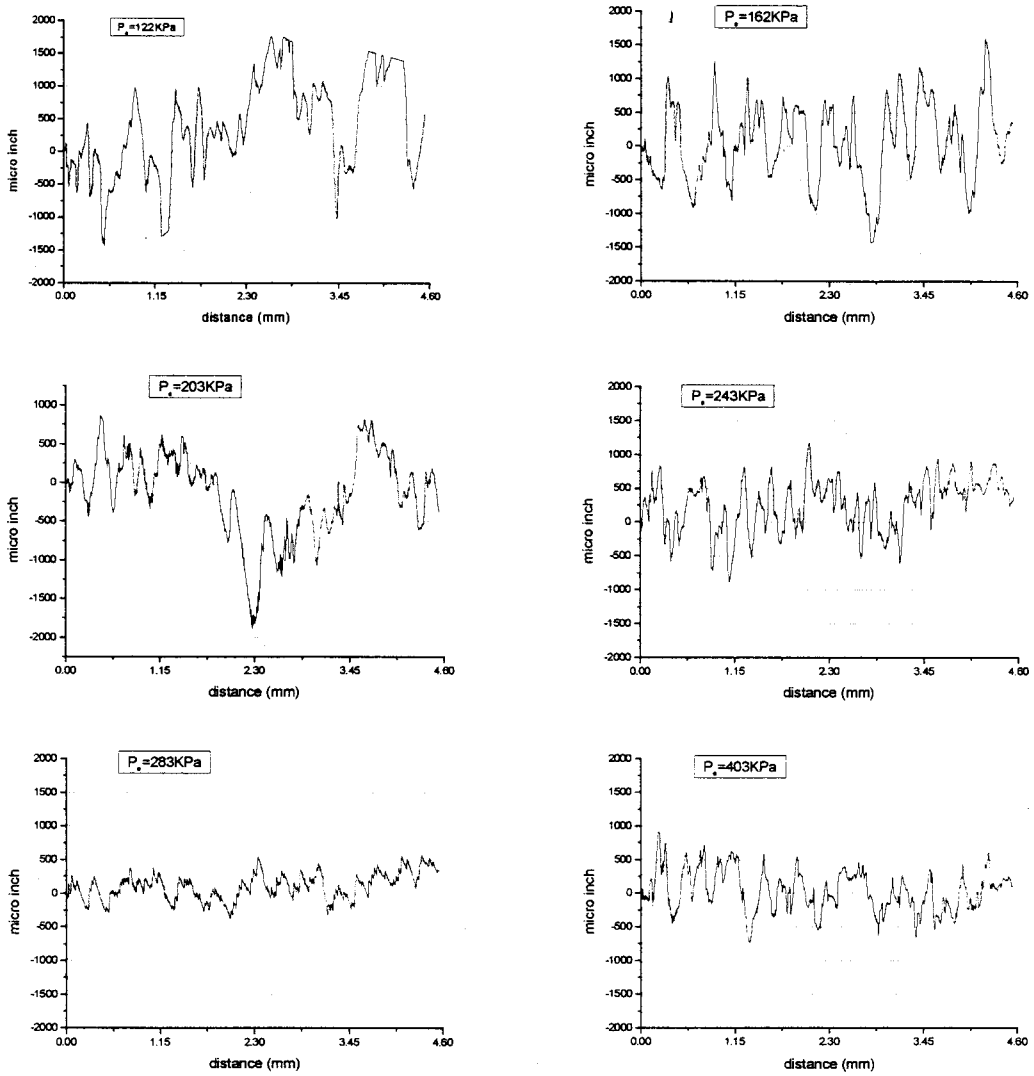

Fig. 15 Profilometer measurements of cut surface with different gas pressure at 2.0 mm standoff (incomplete cuts at $P_e = 323$ kPa, $P_e = 363$ kPa)

three-dimensional. However, since the geometric size of the kerf width is much smaller than the nozzle diameter, one would expect that the basic shock behavior of the real cutting is similar to that of the axisymmetric case.

Experiments were carried out under the same conditions of the mass flow rate experiments. Cold-rolled mild steel of 1.6 mm thickness was cut using a PRC-1500 CO_2 laser system operated in CW and TEM_{00} mode. In Group-1 experiments, oxygen was used for cutting, H was fixed at 2.0 mm and P_e was varied from 122 kPa to 403 kPa. In Group-2 experiments, air was used as assist gas for cutting, P_e was fixed at 363 kPa and H was varied. The experimental conditions are as follows:

	Power	Cutting Speed	H	P_e
Group-1	200 W	37 mm/s	2.0 mm	varies
Group-2	800 W	37 mm/s	varies	363 kPa

To compare cut quality distinctively, the laser power and cutting speed were adjusted so that some samples were barely cut through or not through.

In Group-1 experiments, the samples were not cut through for $P_e = 323$ kPa, 363 kPa. To quantify the surface roughness, measurements were taken using a profilometer along a line 0.2 mm from the bottom. The profilometer traces at different gas pressure levels are shown in Fig. 15. As seen, the surface finish has relatively higher roughness at $Pe = 122$ kPa. The roughness decreases to a minimum value at $P_e = 283$ kPa. The incomplete cases of $P_e = 323$ kPa and $P_e = 363$ kPa can be reasonably considered of highest roughness. The surface roughness again decreases at $P_e = 403$ kPa. The fluctuation of cut surface quality with the gas pressure under fixed standoff distance thus matches the fluctuation pattern of mass flow rate.

In Group-2 experiments, large amount of dross was found clinging to the bottom edge of the cut kerf because air was used as assist gas. Figure 16 shows the dross attachment on cut edge. Dross was observed at $H = 1.0$ mm. The amount of dross increases for $H = 1.5$ mm. Cuts were incomplete at $H = 2.0$ and 2.5 mm which is equivalent to extremely severe dross attachment. The dross attachment then suddenly decreases to a minimum amount at $H = 3.0$ mm, and it increases slightly at $H = 3.5$ mm. The sudden decrease of the dross corresponds to the jump of the mass flow rate as described in the previous sections. The variation of dross attachment as varying standoff distance thus follow the same pattern as that of the mass flow rate.

The laser cutting experiments show that the cut quality of roughness and dross attachment are directly influenced by shock structure as presented by variation of mass through rate. The similarity of cut quality variation with variation of gas pressure and standoff distance to those of the mass flow rate in axisymmet-

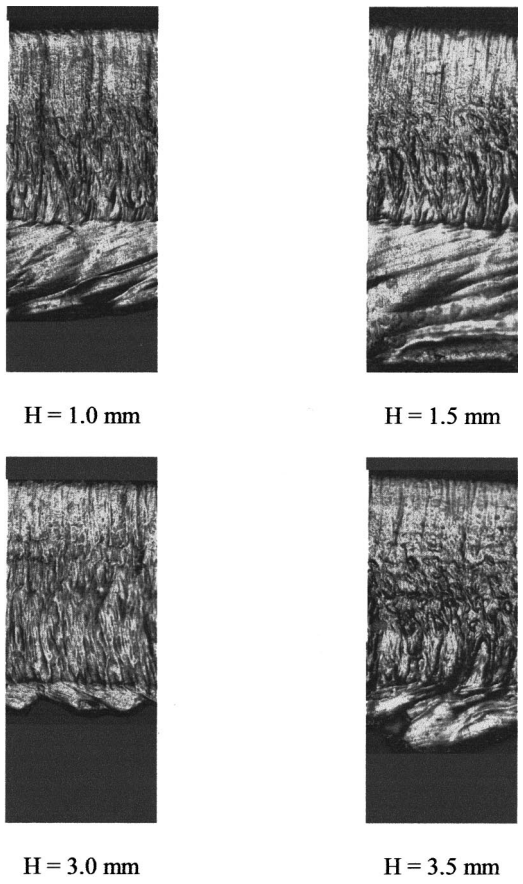

Fig. 16 Dross attachment on cut surface with different standoff (incomplete cuts for $H=2.0$ and 2.5 mm)

ric case indicate that the basic shock structures of real cutting cases are similar to those of axisymmetric cases. Although the effects of melt flow are not taken into account when the shock structures are predicted in the numerical simulation, the cut experiments show that the variation of cut quality conforms their association with shock structure and gas removal capability as predicted.

8 Conclusions

The interaction of a gas jet with the workpiece in laser machining is investigated by systematically studying the influence of the processing parameters on the shock structure of the gas flow. The numerical simulation of a transonic, turbulent jet impinging on a plate (workpiece) with a hole concentric with the jet is presented, revealing the effects of gas pressure and nozzle standoff distance on shock structure. Experimental measurements of the mass flow rate through the hole under conditions corresponding to those of the simulation were carried out. Experimental data are found to match the simulation results. It is found that certain favorable operating conditions exist under which the oblique incident shock waves merges on the centerline and reflect before interacting with the normal standoff shock. In those cases, the total pressure loss across the standoff shock is less and a high total pressure remains at the machining front. The direct interaction of the incident waves and the normal standoff shock results in a large reduction of the total pressure across the standoff shock, conditions unfavorable to laser machining. In addition, the pressure gradient and shear force fluctuate at the machining front, reducing the removal capability of the gas jet and resulting in a poorer surface finish. The experimental results of laser cutting confirm that the cut quality including roughness and dross are affected by the shock structure and removal capability as predicted.

Acknowledgment

This work is supported by a National Science Foundation grant DMI-9500181.

Nomenclature

A = are of delivery nozzle exit
A_m = area of measurement nozzle exit
B = slot width (Test Case 1)
c_D = nozzle discharge coefficient
C_μ = a constant in relationship between μ and $k/\sqrt{\varepsilon}$ (Eq. (4))
d = hole diameter
D = nozzle exit diameter
e = internal energy
$\mathbf{F}$ = vector of x-directed fluxes
$\mathbf{F}_v$ = viscous flux
$\mathbf{G}$ = vector of r-directed fluxes
$\mathbf{G}_v$ = viscous flux
H = standoff distance
k = turbulent kinetic energy
$\dot{m}$ = mass flow rate
M = Mach number
M_j = exit Mach number
p = static pressure
p_t = total pressure
P_e = total gauge pressure at delivery nozzle exit
P_a = ambient pressure
P_j = static pressure at delivery nozzle exit (Test Case 1 and 2)
R = universal gas constant
t = time
T = temperature
T_0 = stagnation temperature
u,v = velocities in x and r directions
u_τ = friction velocity
V_m = velocity at the measurement nozzle exit
x = axial coordinate
y = distance normal to the wall
y^+ = distance normal to the wall in wall units
ρ = density
ρ_m = density at measurement nozzle exit
γ = specific heat ratio
μ = effective viscosity
μ_m = molecular viscosity
μ_t = turbulent viscosity
τ = shear stress
ε = kinetic energy dissipation

Subscripts for $\dot{m}$

n = delivery nozzle
h = hole
j = jet

References

[1] Ivarson, A., et al., 1996, ''The Role of Oxygen Pressure in Laser Cutting Mild Steels,'' J. Laser Appl., **8**, pp. 191–196.
[2] O'Neill, W., and Steen, W. M., 1995, ''A Three-Dimensional Analysis of Gas Entrainment Operating During the Laser-Cutting Process,'' J. Phys. D: Appl. Phys., **28**, pp. 12–18.
[3] Chryssolouris, G., and Choi, W. C., 1989, ''Gas Jet Effects on Laser Cutting,'' CO_2 Lasers and Applications, SPIE, **1042**, pp. 86–96.
[4] Brandt, A. D., and Settles, G. S., 1997, ''Effect of Nozzle Orientation on the Gas Dynamics of Inert-Gas Laser Cutting of Mild Steel,'' J. Laser Appl., **9**, pp. 269–277.
[5] LaRocca, A. V., et al., 1994, ''Nozzle Design to Control Fluid-Dynamic Effects in Laser Cutting,'' SPIE, **2207**, pp. 169–180.
[6] O'Neill, W., et al., ''The Dynamics Behavior of Gas Jets in Laser Cutting,'' Proc. ICALEO'92, pp. 449–458.

[7] Man, H. C., et al., 1997, ''Design of Supersonic Nozzle for Laser Cutting With Pressure Gas,'' Proc. ICALEO'97, Sec. B, pp. 118–127.
[8] Masuda, W., et al., 1994, ''Aerodynamic Characteristics of Underexpanded Coaxial Impinging Jets,'' JSME Int. J., **37**, No. 4, pp. 769–775.
[9] Oosthuizen, P. H., and Carscallen, W. E., 1997, *Compressible Fluid Flow*, The McGraw-Hill.
[10] Addy, A. L., 1981, ''Effects of Axisymmetric Sonic Nozzle Geometry on Mach Disk Characteristics,'' AIAA J., **19**, pp. 121–122.
[11] Ewan, B. C. R., and Moodie, K., 1986, ''Structure and Velocity Measurements in Underexpanded Jets,'' Combust. Sci. Technol., **45**, pp. 275–288.
[12] Abbett, M., 1971, ''Mach Disk in Underexpanded Exhaust Plumes,'' AIAA J., **9**, pp. 512–514.
[13] Carling, J. C., and Hunt, B. L., 1974, ''The Near Wall Jet of a Normally Impinging, Uniform, Axisymmetric, Supersonic Jet,'' J. Fluid Mech., **66**, Part 1, pp. 159–176.
[14] Gummer, J. H., and Hunt, B. L., 1971, Aeronaut. Q., **22**, p. 403.
[15] Ginzburg, I. P., et al., 1973, ''Some Singularities of Supersonic Under-Expanded Jet Interaction With a Plane Obstacle,'' J. Eng. Phys., **19**, p. 1081.
[16] Kalghatgi, G. T., and Hunt, B. L., 1976, ''The Occurrence of Stagnation Bubbles in Supersonic Jet Impingement Flows,'' Aeronaut. Q., **27**, No. 3, pp. 169–185.
[17] Fieret, J., et al., 1987, ''Overview of Flow Dynamics in Gas-Assisted Laser Cutting,'' High Power Lasers, SPIE, **801**, pp. 243–250.
[18] Yakhot, V., and Orszag, S. A., 1986, ''Renormalization Group Analysis of Turbulence: I. Basic Theory'', J. Sci. Comput., **1**, No. 1, pp. 1–51.
[19] Roe, P. L., 1986, ''Characteristic Based Schemes for the Euler Equations,'' Annu. Rev. Fluid Mech., **18**, pp. 337–365.
[20] Stratford, B. S., 1964, ''The Calculation of the Discharge Coefficient of Profiled Choked Nozzles and the Optimum Profile for Absolute Air Flow Measurements,'' J. R. Aeronaut. Soc., **68**, No. 640, pp. 237–245.
[21] Holman, J. P., 1984, *Experimental Methods for Engineers*, McGraw-Hill.
[22] Seiner, J. M., and Norum, T. D., 1979, ''Experiments of Shock Associated Noise on Supersonic Jets,'' AIAA Paper 79-1526.
[23] Iwamoto, J., 1990, ''Impingement of Under Expanded Jets on a Flat Plate,'' ASME J. Fluids Eng., **112**, pp. 179–184.